The Astrophysical Journal, 821:122 (15pp), 2016 April 20 doi:10.3847/0004-637X/821/2/122

A COHERENT STUDY OF EMISSION LINES FROM BROADBAND PHOTOMETRY: SPECIFIC STAR FORMATION RATES AND [O III]/Hβ RATIO AT $3 < z < 6$

A. L. Faisst[1,2], P. Capak[1,2], B. C. Hsieh[3], C. Laigle[4], M. Salvato[5], L. Tasca[6], P. Cassata[6], I. Davidzon[6,7], O. Ilbert[6], O. Le Fèvre[6], D. Masters[1,2], H. J. McCracken[4], C. Steinhardt[1,2], J. D. Silverman[8], S. de Barros[7], G. Hasinger[9], and N. Z. Scoville[2]

[1] Infrared Processing and Analysis Center, California Institute of Technology, Pasadena, CA 91125, USA; afaisst@ipac.caltech.edu, Twitter: @astrofaisst
[2] Cahill Center for Astronomy and Astrophysics, California Institute of Technology, Pasadena, CA 91125, USA
[3] Academia Sinica, Institute of Astronomy & Astrophysics, P.O. Box 23-141, Taipei 10617, Taiwan
[4] Institut d'Astrophysique de Paris, CNRS & UPMC, UMR 7095, 98 bis Boulevard Arago, F-75014, Paris, France
[5] Max Planck Institut für Extraterrestrische Physik, Giessenbachstrasse 1, D-85748, Garching bei München, Germany
[6] Aix Marseille Université, CNRS, LAM (Laboratoire d'Astrophysique de Marseille) UMR 7326, F-13388, Marseille, France
[7] INAF—Osservatorio Astronomico di Bologna, via Ranzani 1, I-40127, Bologna, Italy
[8] Kavli Institute for the Physics and Mathematics of the Universe (WPI), The University of Tokyo Institutes for Advanced Study, The University of Tokyo, Kashiwa, Chiba 277-8583, Japan
[9] Institute for Astronomy, 2680 Woodlawn Dr., University of Hawaii, Honolulu, HI 96822, USA
Received 2016 January 15; accepted 2016 March 7; published 2016 April 20

ABSTRACT

We measure the Hα and [O III] emission line properties as well as specific star formation rates (sSFRs) of spectroscopically confirmed $3 < z < 6$ galaxies in COSMOS from their observed colors versus redshift evolution. Our model describes consistently the *ensemble of galaxies* including intrinsic properties (age, metallicity, star formation history), dust attenuation, and optical emission lines. We *forward-model* the measured Hα equivalent widths (EW) to obtain the sSFR out to $z \sim 6$ without stellar mass fitting. We find a strongly increasing rest-frame Hα EW that is flattening off above $z \sim 2.5$ with average EWs of 300–600 Å at $z \sim 6$. The sSFR is increasing proportionally to $(1+z)^{2.4}$ at $z < 2.2$ and to $(1+z)^{1.5}$ at higher redshifts, indicative of a fast build-up of mass in high-z galaxies within e-folding times of 100–200 Myr at $z \sim 6$. The redshift evolution at $z > 3$ cannot be fully explained in a picture of growth driven by cold accretion. We find a progressively increasing [O III]λ5007/Hβ ratio out to $z \sim 6$, consistent with the ratios in local galaxies selected by increasing Hα EW (i.e., sSFR). This demonstrates the potential of using "local high-z analogs" to investigate the spectroscopic properties and relations of galaxies in the re-ionization epoch.

Key words: galaxies: evolution – galaxies: high-redshift – galaxies: star formation

1. INTRODUCTION

With current broad-band near- to mid-infrared (IR) filters on ground- and space-based telescopes we are able to select galaxy samples in the very early epochs of the universe. However, the study of their physical properties—essential to refine our understanding of the formation and evolution of galaxies—is hampered by several technical problems.

In recent years, a lot of progress has been made in understanding galaxy formation in the early universe before the peak of the cosmic star formation density at $z \sim 2-3$. In particular, several new avenues have been opened by large spectroscopic and photometric campaigns to explore the near- to mid-IR wavelength range over large parts of the sky. From these, it became clear that galaxies live on a so-called "main sequence" connecting their stellar mass with their star formation rate (SFR) out to redshifts as high as $z \sim 5$ (Speagle et al. 2014; Steinhardt et al. 2014; Tasca et al. 2015). Also, it is suggested that galaxies grow very rapidly in the early universe due to high gas fractions and/or star formation efficiencies (e.g., Scoville et al. 2016; Silverman et al. 2015a). Going in hand with the former, a marginal flattening of the relation between metallicity and stellar mass is expected for young galaxies at $z \sim 5$ (see Faisst et al. 2015). These recent observations have triggered questions that have yet to be answered. For example, galaxies have been found that are more massive than expected from hierarchical assembly of dark-matter haloes (e.g., Steinhardt et al. 2015). The formation of such massive galaxies at high redshifts requires their fast growth and therefore an increase in the specific SFR (sSFR = SFR/M, a measure for the rate of build-up of mass in galaxies) at $z > 3$ (e.g., Weinmann et al. 2011). This increase is also predicted in the picture of accretion-dominated galaxy growth (e.g., Dekel et al. 2009; Tacchella et al. 2013) and recent hydrodynamical simulations (e.g., Davé et al. 2011; Sparre et al. 2015). Some studies observe these predictions (Stark et al. 2013; de Barros et al. 2014; Jiang et al. 2016), while others find a considerable flattening of the sSFR at $z > 3$ (González et al. 2014; Marmol-Queralto et al. 2015; Tasca et al. 2015). Finally, relations based on local galaxies, e.g., the relations between metallicity and strong emission lines, may no longer be applicable at higher redshifts due to the change in internal physical processes in such galaxies such as ionization or the abundance of [N II] (e.g., Masters et al. 2014; Steidel et al. 2014; Cowie et al. 2016; Shapley et al. 2015).

Stellar mass and SFRs as well as metallicity and ionization parameter are the most important basic physical quantities on which the above results are based and the above questions depend. While these can be measured reliably at low redshifts by a good multi-wavelength coverage in imaging and spectroscopy, there are several caveats at higher redshifts. First, SFRs have to be measured in the UV, because reliable estimators such as the Hα emission line are out of spectral coverage. The UV is highly sensitive to dust attenuation (e.g., Bouwens et al. 2012b), which shows a large diversity in high-redshift

galaxies (see Capak et al. 2015). Second, deep observed mid-IR imaging data are necessary to probe the old stellar populations in galaxies at $z > 4$ and therefore allow a reliable measurement of stellar masses. Third, mid-IR filters at these redshifts are contaminated by the (unknown) contribution of strong emission lines (with increasing strength at higher redshifts, see Khostovan et al. 2015), which boost the masses significantly (e.g., Schaerer & de Barros 2009; Stark et al. 2013; de Barros et al. 2014). Finally, the conversion from the observed data to these quantities (i.e., stellar mass and SFR) depends on theoretical models of the intrinsic properties of galaxies such as their age, metallicity, and star formation history (SFH), all of which are not known a priori for individual galaxies at high redshifts.

In this paper, we develop a model-insensitive way to measure the sSFR and the emission line strength at $3 < z < 6$ from primary observables. Furthermore, we demonstrate the potential of using local high-z analogs to probe the spectral properties of high-redshift galaxies up to $z = 6$. In particular, we use the redshift evolution of the galaxy population with averaged observed near- to mid-IR color to measure the Hα equivalent width (EW), from which we directly derive the sSFR(z). The measurement of the EW has two parts, namely the measurement of the observed flux/color and the estimation of the underlying continuum between 4500 and 6500 Å underneath optical emission lines. The latter we *forward-model* by assuming intrinsic properties of the galaxies (dust attenuation, metallicity, stellar population age, star formation history) and we show that the resulting continuum is very insensitive to the choice of these parameters in the above-specified wavelength range. The determination of the Hα EW from observed galaxy colors has been used in the past (Shim et al. 2011; Stark et al. 2013; Marmol-Queralto et al. 2015; Rasappu et al. 2015; Smit et al. 2015a, 2015b), but mostly at discrete redshift bins and for small sample sizes. We perform here a consistent analysis across a large redshift range with a much larger sample of spectroscopically confirmed galaxies than in previous studies. Our large sample allows us to model the *ensemble of galaxies* instead of considering single galaxies. This enables us to marginalize over the (poorly known) intrinsic properties of the galaxies when modeling the continuum below the optical emission lines. It also gives us a convenient way to describe the scatter (systematic and physical) of the ensemble's properties; we can propagate this through our model and investigate its effect on our results.

The plan for this paper is as follows. In Section 2 we describe the sample of spectroscopically confirmed galaxies that is used for this analysis. In Section 3 we describe the modeling of the observed color versus redshift relation including the contribution of intrinsic parameters (age, metallicity, SFH), dust attenuation, and optical emission lines. In the results section (Section 4), we derive the redshift evolution of the Hα EW, the sSFR(z), as well as the [O III]/Hα ratio out to $z \sim 6$. These results are discussed in Section 5 and summarized in Section 6.

Throughout this work we adopt a flat cosmology with $\Omega_{\Lambda,0} = 0.7$, $\Omega_{m,0} = 0.3$, and $h = 0.7$. Magnitudes are given in the AB system (Oke & Gunn 1983) and all masses are scaled to a Chabrier (2003) initial mass function (IMF).

2. DATA AND SAMPLE SELECTION

2.1. Data

In this work, we use the two square degrees of the Cosmic Evolution Survey (COSMOS, Scoville et al. 2007) field, which are observed by a wealth of instruments in imaging as well as spectroscopy across a broad range of wavelengths. We make use of the following data sets.

1. The COSMOS spectroscopy catalog, which contains more than 6000 high-quality spectra at $1 < z < 6$ (M. Salvato 2016, private communication).
2. The VIMOS Ultra Deep Survey (VUDS) spectroscopy catalog, containing galaxy spectra at $2 < z < 6$ (Le Fèvre et al. 2014).
3. The *COSMOS2015* photometric catalog including photometry from the UV to mid-IR as well as photometric redshifts and stellar masses (Laigle et al. 2016).

The COSMOS spectroscopic master catalog available to the COSMOS collaboration is a compilation of all spectroscopic observations up to $z \sim 6$ that are carried out on the COSMOS field. The galaxy sample is selected in different ways (color, photometric redshift, Lyman break technique) and observed by several different instruments depending on the redshift (VIMOS, FORS2, FMOS, MOIRCS, DEIMOS, MOSFIRE). The different selection techniques lead to a large coverage of physical properties of the galaxies, thus this sample represents well the population of star-forming galaxies at these redshifts. For more information, we refer to the official COSMOS webpage.[10]

The VUDS spectroscopy catalog contains galaxies selected by photometric redshifts with a flux limit of $i_{\rm AB} = 25$. The spectra are obtained with the VIMOS spectrograph on the ESO Very Large Telescope (Le Fèvre et al. 2003). For more information, we refer to Le Fèvre et al. (2015).

The *COSMOS2015* photometric catalog contains the photometry of the extracted galaxies on COSMOS measured from the UV to the mid-IR images. The source extraction is based on a χ^2 image determined from the Subaru z-band and the COSMOS/UltraVISTA *YJHK* bands (see Capak et al. 2007; McCracken et al. 2012; Ilbert et al. 2013). Part of this catalog is the mid-IR data at 3.6 and 4.5 μm down to ~25.5 mag (3σ in $3''$ diameter; as of 2015 October) from the *Spitzer Large Area Survey with Hyper-Suprime-Cam* (SPLASH, Steinhardt et al. 2014).[11] These sources are extracted using the segmentation map of the *COSMOS2015* catalog and an improved version of IRACLEAN (Hsieh et al. 2012) in order to overcome the source confusion (blending).

We subsequently match the photometry catalog with the spectroscopy catalogs within $1''$ radius in order to recover the photometry for our spectroscopically confirmed galaxies. More than 97% of the galaxies are matched within a radius of $0\farcs3$.

2.2. Galaxy Selection, Redshift, and Stellar Mass Distribution

For the purpose of this work, we apply a very stringent cut to our sample in terms of spectroscopy as well as photometry. We include only reliable spectroscopic redshifts in our sample (>80% probability of correct spectroscopic redshift) at $1 < z < 6$ and remove spectroscopically confirmed active

[10] http://cosmos.ipac.caltech.edu
[11] http://splash.caltech.edu

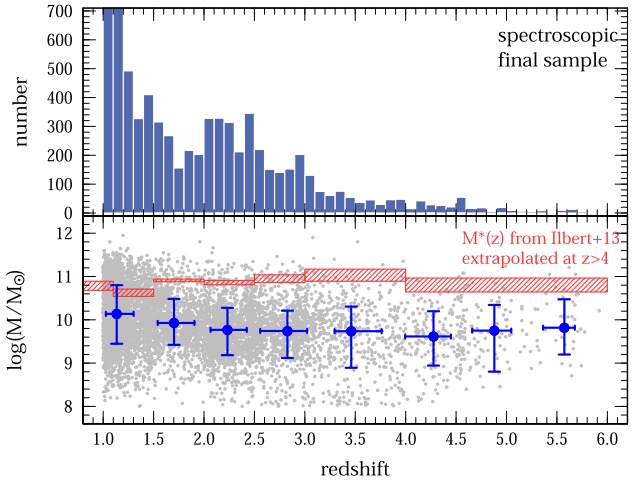

Figure 1. Properties of our final sample (galaxies clear of contamination within 2″). Top: redshift distribution of our final spectroscopic sample. Bottom: stellar mass distribution as a function of redshift for our final spectroscopic sample of galaxies (see Laigle et al. 2016). The gray points show individual galaxies and the blue symbols show the mean $\log(M/M_{\odot})$ in redshift bins, with 68% percentiles in redshift and mass shown by the error bars. The red-hatched bars show the value of the Schechter function M^{*} from Ilbert et al. (2013), extrapolated at redshifts $z > 4$.

galactic nuclei based on their broad optical emission. We will use the redshift range $1 < z < 3$ to verify our method by direct comparison of our results to spectroscopic emission line measurements. The measurement of colors depends strongly on source confusion, which commonly is taken into account during the extraction of the galaxy photometry. For the purpose of this work, we add additional security and remove potentially blended sources in the near- to mid-IR by directly checking their number of neighboring galaxies. For this purpose, we use the high-resolution F814W (*I*-band) images from the *Hubble Space Telescope*'s Advanced Camera for Surveys (*HST*/ACS), as well as the COSMOS/UltraVISTA optical/near-IR selected catalog. We extract the number of companions within a certain aperture size for each galaxy in our sample. Given the PSF aperture size of ∼2″–3″ in the mid-IR, we remove all the galaxies with companions closer than 2″ and 3″ in radius, respectively.

Our final sample at $1 < z < 6$ with no contamination of neighboring galaxies within a radius of 2″ (3″) contains more than 4000 (1500) galaxies in total. In the following analysis we use the galaxy sample clear of neighbors within 2″. The results do not change significantly if we use the more restricted sample of galaxies without contamination within 3″ radius (although the uncertainties are larger because of the greatly decreased number of galaxies). In particular, in the redshift range $3 < z < 6$, we use 530 spectroscopically confirmed galaxies. Figure 1 shows the redshift and stellar mass distribution of our final sample of galaxies (without contaminants within 2″) along with the Schechter function M^{*} values from Ilbert et al. (2013), extrapolated beyond $z = 4$ as a reference. The stellar masses are measured on the *COSMOS2015* photometry using the spectral energy distribution (SED) fitting routine `Le Phare`[12] including the fitting of emission lines set proportional to the UV flux (Laigle et al. 2016). We expect our galaxies to have a median stellar mass of $\log(M/M_{\odot}) \sim 9.8$ at $z > 3$. Our sample is one order of magnitude less massive than the expected characteristic stellar mass M^{*} of the Schechter function at $1.5 < z < 6$, thus probing the low end of the stellar mass distribution at these redshifts. We stress that the goal of this paper is to access the sSFR from primary measurements (galaxy color) and we therefore do not use these stellar masses in the following. They serve only to visualize the expected mass range of our sample of galaxies and the comparison to other studies.

[12] See Ilbert et al. (2006) and http://www.cfht.hawaii.edu/~arnouts/LEPHARE/.

3. EMISSION LINE STRENGTHS FROM OBSERVED COLORS

In this section, we describe in detail our model including intrinsic galaxy properties (age, metallicity, SFH), dust attenuation, and optical emission lines. From this we derive model galaxy colors as a function of redshift, which are compared to the observed colors versus redshift evolution in our galaxy sample. This allows us, using a minimization algorithm, to solve for the spectral properties of the ensemble of these galaxies in specific redshift windows, which are detailed in the following.

3.1. Redshift Windows and Colors

The idea of this paper is to constrain the emission line properties of galaxies from their observed colors. Emission lines contribute to different broad-band filters for galaxies at different redshifts. This produces "wiggles" in the observed color–redshift evolution with respect to what is expected from a continuum without nebular lines. However, the observed color of a galaxy is affected not only by emission lines, but also by its intrinsic properties (age, metallicity, SFH) and dust attenuation. These change with redshift and thus are degenerate with the effects of emission lines. In a later section we will discuss how much these various properties affect the observed color of a galaxy. In order to separate the effect of emission lines, we have to calibrate our model in redshift ranges in which the continuum flux in broad-band filters is free of emission lines and thus reveals the intrinsic color and dust attenuation.

Figure 2 shows the location of strong emission lines (Hα, Hβ, [O II], and [O III]) in different near- and mid-IR broad-band filters as a function of redshift. There are several different redshift ranges (labeled for the case $3 < z < 6$ and mid-IR colors):

1. Redshift ranges free of emission lines that reveal the intrinsic color and dust attenuation of the galaxies and thus anchor our model (box labeled "intrinsic/dust").
2. Redshift ranges where the observed color includes the Hα emission line and thus allows us to measure EW(Hα) (box labeled "Hα").
3. Redshift ranges that allow the measurement of the ratio [O III]/Hα (box labeled "[O III]/Hα").

These different redshift ranges exist for different observed colors and can be bundled into larger redshift windows. For the purpose of this work, we choose three different redshift windows, each with a corresponding observed color.

(A) $1.0 < z < 2.9$ in observed $[H] - [K]$ color,
(B) $1.0 < z < 4.0$ in observed $[K] - [3.6\ \mu\text{m}]$ color, and
(C) $3.0 < z < 6.0$ in observed $[3.6\ \mu\text{m}] - [4.5\ \mu\text{m}]$ color.

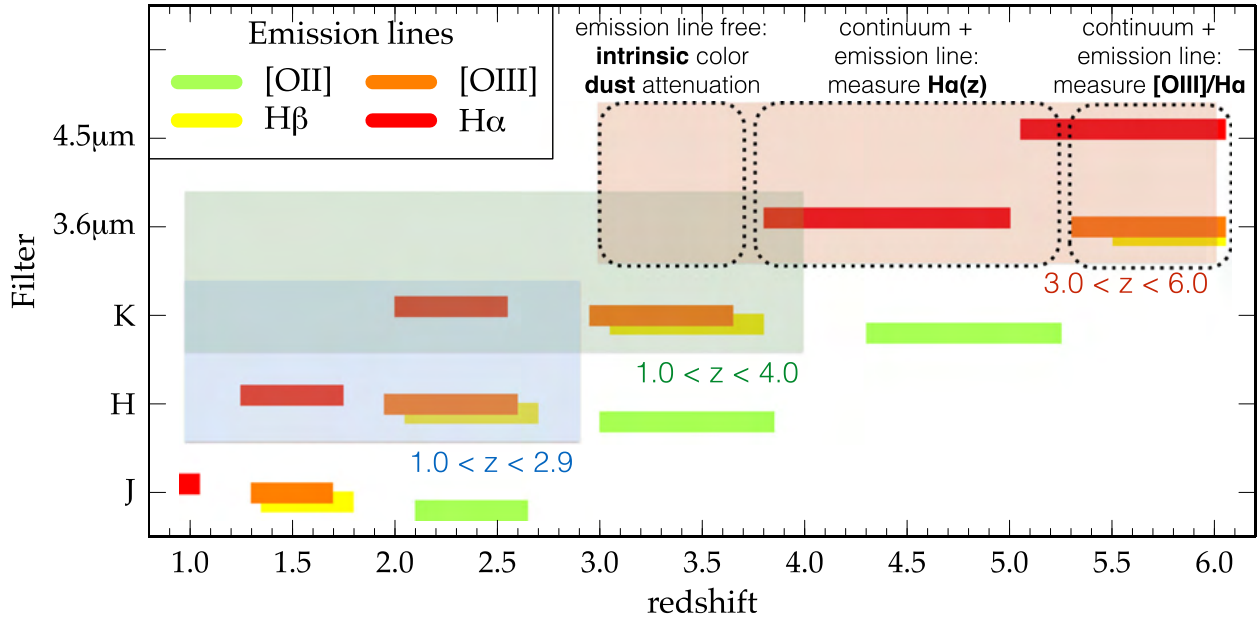

Figure 2. Contribution of different optical emission lines ([O II], green; [O III], orange; Hα, red; Hβ, yellow) to broad-band filters as a function of redshift. The blue, green, and red bands show the three redshift windows (redshifts indicated) to which we apply our emission line + dust model to estimate the Hα EW as well as the [O III]/Hα line ratio. The dotted boxes show, for the $3 < z < 6$ window as a textbook case, how redshift ranges are used to reveal the intrinsic color + dust attenuation (used to anchor our model fit), the EW(Hα) vs. redshift evolution, and the ratio [O III]/Hα.

Each of the three redshift windows is designed to have a redshift range free of emission lines to anchor the model to the intrinsic color. Furthermore, this choice allows us to consistently model EW(Hα) across the redshift range $1 < z < 6$ and the Hα/[O III] ratio at $z \sim 2.2$, $z \sim 3.3$, and $z \sim 5.5$. The redshift windows (A) and (B) are used to verify our method by comparing our results to spectroscopic measurements. Given the strong dependence of the 4000 Å Balmer break on stellar population properties, we do not model the [O II] emission line here. Fortunately, the wavelength part redward of the [O II] emission is relatively insensitive to the intrinsic properties of the stellar population as we will discuss later.

3.2. Modeling the Mean Observed Color as a Function of Redshift

The observed color of a galaxy is affected threefold by its properties: (i) by its intrinsic color (age, metallicity, SFH), (ii) by the dust attenuation, and (iii) by emission lines.

In the following sections, we build up a model for the observed color in the different redshift windows from these three contributions. From its comparison to the true observed colors, we can then compute the average emission line properties of our galaxies. It is important to note that the intrinsic galaxy properties as well as dust are solely used to represent the continuum under the Hβ, [O III], and Hα lines, i.e., redward of the 4000 Å break. In particular, the fitting of our model continuum to the observed continuum in line-free wavelength regions using the contribution from dust as a "knob" (Section 3.2.2) smooths out possible variations in the intrinsic galaxy properties that are missed elsewhere in our model. This is the main advantage of our forward-modeling technique and allows the robust estimation of the emission line properties as we show in the following.

3.2.1. The Intrinsic Color (Age, Metallicity, SFH)

For describing the intrinsic color of a galaxy population, we have to assume a metallicity, stellar population age, and SFH. These are unknown a priori, therefore we set up a grid that brackets reasonable choices of these parameters. Our forward-modeling technique then allows us to investigate the effects on the resulting observed color and the results derived in this work. As a basis we use the composite stellar population library from Bruzual & Charlot (2003) with a Chabrier IMF and create SEDs with different SFHs, metallicities, and ages using GALAXEV.[13]

Galaxies up to $z \sim 4$–5 show a tight relation between SFR and stellar mass, which leads to an exponentially increasing SFH for the average population of galaxies (Daddi et al. 2007; Noeske et al. 2007; Speagle et al. 2014; Steinhardt & Speagle 2014; Smit et al. 2015b). We bracket possible histories by a constant SFH, a delayed exponentially decreasing SFH (SFR $\propto t/\tau_p^2 \times \exp(-t/\tau_p)$) with a peak at $\tau_p = 1$ Gyr, and an exponentially increasing SFH (SFR $\propto \exp(t/\tau)$) with an e-folding time of $\tau = 500$ Myr. Furthermore, galaxies at high redshift show a considerably lower metallicity content (e.g., Erb et al. 2006; Maiolino et al. 2008; Mannucci et al. 2009; Faisst et al. 2015). We therefore bracket the range in metallicity between $Z = 0.004$ (1/5th of solar) and $Z = 0.02$ (solar). However, because of the minor effect of metallicity on the continuum, we keep it constant with redshift. Finally, we assume the age of the galaxy to be the time since the estimated start of re-ionization at $z = 11$ (e.g., Planck Collaboration et al. 2015). Similar parameterizations of the galaxy's age as a function of redshift (e.g., half of the Hubble time) do not change our results.

In Figure 3, we show the effect of intrinsic properties as well as dust attenuation on the observed [3.6 μm] − [4.5 μm] color

[13] See Bruzual & Charlot (2003) and http://www.bruzual.org/.

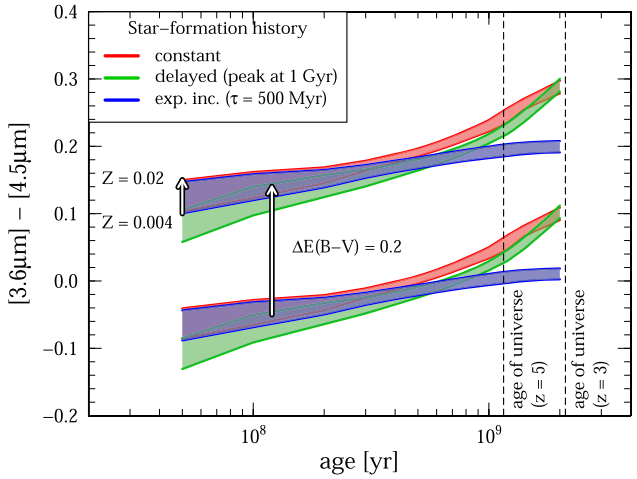

Figure 3. Effect of intrinsic properties (metallicity, age, SFH) and dust on the observed [3.6 μm] − [4.5 μm] color in the case of a $z = 5$ galaxy. Metallicity plays only a minor role in setting the color of a galaxy (see arrow from 1/5th of solar to solar). The colored bands show three different SFHs (constant, delayed, and exponentially increasing). Clearly, dust attenuation (ranging between $E(B-V) = 0.1$–0.4 mag in our sample, depending on redshift) is the dominant contributor to color, followed by the SFH for galaxies older than ∼1 Gyr (or $z < 5$). Importantly, the color is insensitive to reasonable SFHs and stellar population ages for young (<1 Gyr) galaxies at high redshifts.

for the example of a galaxy at $z = 5$. First, we emphasize the small effect of metallicity on the continuum: a change from 1/5th of solar to solar metallicity results in a change of less than 0.05 mag in color. Second, in the case of an exponentially increasing SFH with $\tau = 500$ Myr, the observed color as a function of age reddens less than 0.1 mag for all possible ages of a $z = 5$ galaxy. In the case of a constant and delayed SFH, the reddening is stronger due to domination by old stars with increasing age, but less than 0.2 mag over a time of ∼2 Gyr, which corresponds to $z \sim 3$. Compared to this, the reddening by dust is of similar or larger amplitude (common dust extinctions are of the order of $E(B-V) \sim 0.1$–0.4 mag in our sample). Note that the model uncertainties are significantly reduced at high redshifts. First, the observed color is mostly independent of SFH for young galaxies with ages of less than ∼1 Gyr, i.e., $z > 5$. Second, it is expected that galaxies at high redshifts are dust-poor (e.g., Dunlop et al. 2013; Bouwens et al. 2014; Capak et al. 2015). Third, their age and metal content are well defined because of the young age of the universe at that time.

Summarizing, we find that the expected reddening by dust exceeds the effect of metallicity as well as SFH and age for young galaxies up to ∼1 Gyr in age (corresponding to $z > 5$). For galaxies with a constant or exponentially declining SFH, as is the case at lower redshifts, we expect the intrinsic color to change more significantly with age. Also the color starts to depend increasingly on the assumed SFH for older galaxies and therefore lower redshifts. Finally, we note that a different IMF does not change these conclusions. For example, using a Salpeter IMF changes the observed color by less than 0.01 mag at a given age.

3.2.2. Emission Lines and Dust

Besides intrinsic properties, dust attenuation and emission lines contribute to the observed color of a galaxy. We derive all rest-frame UV and optical emission lines relative to Hα, which we vary in our model. In detail, we parameterize the evolution of the (rest-frame) Hα EW as

$$\mathrm{EW(H}\alpha) = \mathrm{EW(H}\alpha)_0 \times (1+z)^{\alpha}, \quad (1)$$

where $\mathrm{EW(H}\alpha)_0$ and α are free fitting parameters.

Furthermore, we assume a constant (with redshift) line flux ratio $\mathrm{H}\alpha/[\mathrm{O\,III}] = \xi$ within each of the three redshift windows (see Section 3.1), because [O III] enters only in a narrow redshift range at $z \sim 2.2$, 3.3, and 5.5 for windows (A), (B), and (C), respectively. In our case, [O III] denotes the blended doublet and we assume $[\mathrm{O\,III}]\lambda5007/[\mathrm{O\,III}]\lambda4960 = 3$.

The Hβ line flux is determined from Hα assuming case (B) recombination,

$$f(\mathrm{H}\alpha)/f(\mathrm{H}\beta) = 10^{0.4\times E(B-V)_{\mathrm{neb}}\times(k_\beta - k_\alpha)} \times 2.86, \quad (2)$$

where k_β and k_α are the coefficients for a given dust attenuation curve (we assume here that of Calzetti et al. 2000)[14] at the wavelengths of Hα and Hβ, respectively. The (stellar) dust extinction $E(B-V)_{\mathrm{stel}}$[15] is parameterized as an exponentially decreasing function of redshift (e.g., Hayes et al. 2011),

$$E(B-V)_{\mathrm{stel}} = E(B-V)_0 \times e^{-z/z_{d,0}} \quad (3)$$

with $E(B-V)_0$ and $z_{d,0}$ as free parameters. We also model weaker optical emission lines (e.g., [S II], [N II], He I), which we scale relative to the Hβ line fluxes according to Anders & Fritze-v. Alvensleben (2003), assuming reasonable metallicity between 1/5th solar and solar. Although not particularly strong in emission, these add up and can contribute up to 20% to fluxes in the broad-band filters.

The contributions of dust and emission lines are added to the intrinsic continuum described in the previous section. The emission lines are added assuming a full width at half maximum (FWHM) of 10 Å for the strong (Hα, Hβ, [O II], [O III]) and 5 Å for weak emission lines. Note that because of the large width of the broad-band filters, different (reasonable) choices of FWHM do not change the following results. The model colors are obtained by convolution of the generated SED with the corresponding filter transmission curves (*Spitzer*/IRAC for 3.6 and 4.5 μm and VISTA *H* and *Ks* bands).

3.2.3. Fitting the Observed Color as a Function of Redshift

The top panel in Figure 4 shows the observed color in redshift window (C), i.e., $3 < z < 6$. The other two redshift windows are shown in Appendix B. The symbols show individual galaxies (split into galaxies with no contamination within 2″ and within 3″ radius) and the blue band shows the running mean observed color (including 1σ scatter) as a function of redshift. In the following, we fit this observed color versus redshift evolution with the previously described model for a given combination of metallicity and SFH. We use a Levenberg–Marquardt (LM) algorithm as part of the `R/minpack.lm` package[16] and proceed in two steps.

[14] Several studies indicate that high-redshift galaxies follow a dust attenuation curve similar to that of the Small Magellanic Cloud. However, our model and data are not accurate enough to disentangle the effect of different attenuation curves.

[15] We assume $E(B-V)_{\mathrm{neb}} = E(B-V)_{\mathrm{stel}}/0.76$ (Kashino et al. 2013). However, using a factor close to unity as suggested by more recent studies (Cullen et al. 2014; de Barros et al. 2015; Shivaei et al. 2015) does not affect the results of this paper.

[16] https://cran.r-project.org/web/packages/minpack.lm/index.html

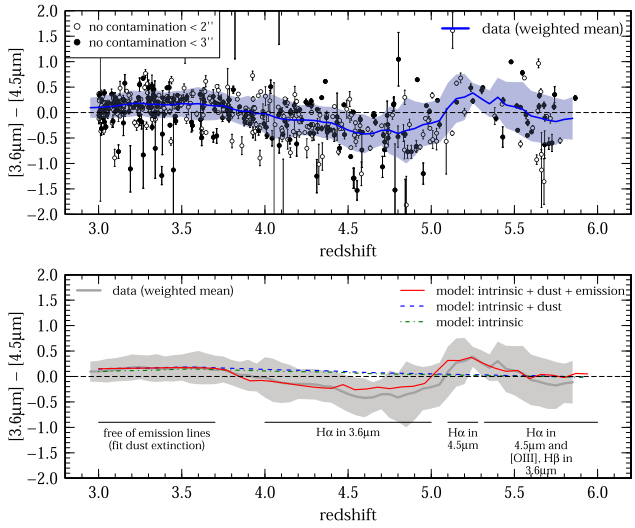

Figure 4. Top: observed color vs. redshift relation at $z > 3$. The open (filled) symbols denote galaxies with no contamination from companions within a radius of 2″ (3″) in ACS/F18W and ground-based data. The blue line shows the weighted mean relation with scatter (light blue band) for galaxies with no companion within 2″. Bottom: the best-fit intrinsic (green, dotted–dashed), intrinsic + dust (blue, dashed), and best-fit (red, solid) models.

1. We fit the dust attenuation as a function of redshift (Equation (3)) in regions devoid of emission lines (see Figure 2). As mentioned above, this fit also includes intrinsic changes of the SED that are not taken into account elsewhere in our model. The sole purpose of this is to model the continuum below the optical emission lines (Hβ, [O III], Hα).
2. We fix the values of $E(B-V)_0$ and $z_{d,0}$ and fit the remaining parameters EW(Hα)$_0$, α, and ξ describing the emission lines.

This procedure is important to break the degeneracies between the effects of dust attenuation and emission lines on the observed color. We find that this is especially important at lower redshifts where galaxies show a significant amount of dust but much weaker EWs compared to high-z galaxies.

We perform these two steps for a total of four combinations describing our intrinsic SED: 1/5th of solar and solar metallicity and two SFHs (constant and exponentially increasing).[17] The bottom panel in Figure 4 visualizes the fit for a constant SFH with solar metallicity at $3 < z < 6$. The best-fit model (intrinsic + dust + emission lines) in solid red is shown along with the dust-reddened intrinsic color (blue dashed), and the intrinsic color (green dotted–dashed). The horizontal lines label what affects the observed color in a given wavelength region (see also Figure 2). The best-fit parameters for each redshift window and intrinsic SED are listed in Table 1.

4. RESULTS

The model described in the previous section allows us to fit the redshift dependence of the Hα EW as well as the [O III]/Hα line ratio from the observed color versus redshift evolution. Furthermore, we are able to derive the sSFR(z) from the former. The results are detailed in the following sections.

[17] The delayed exponentially decreasing SFH yields similar results to a constant SFH and we do not list it here.

4.1. The EW(Hα) Out to z ∼ 6

Figure 5 shows the redshift evolution of EW(Hα) for each of the three redshift windows $1.0 < z < 2.9$, $1 < z < 4$, and $3 < z < 6$ (color-coded bands in blue, green, and red). We overlay the results from the four combinations of metallicity and SFH to show how our choice of intrinsic galaxy properties affects the results. As expected, the differences are negligible, verifying that the observed color is mainly driven by the contribution of emission lines (and dust), see Figure 3. The points color-coded in the same way show EW(Hα) in the redshift ranges where it can be directly measured (see also Figure 2). At $z > 3$, we also show the results for a sample of galaxies selected by photometric redshifts (red squares). The EWs are consistent with our spectroscopic sample, suggesting that it is not severely biased toward young galaxies with enhanced star formation (see also Section 5.1).

Our derived EW(Hα) in the redshift windows (A) and (B) are in excellent agreement with direct determinations from spectroscopy at $z < 3$ obtained by Erb et al. (2006) at ($z \sim 2$), Fumagalli et al. (2012) (at $1 < z < 2$ as part of 3D-*HST*; van Dokkum et al. 2011, p. 74; Brammer et al. 2012; Skelton et al. 2014), and Lamareille et al. (2009) (at $z \sim 0.5$, as part of VVDS; Le Fèvre et al. 2005). Together with these studies based on spectroscopic measurements of the Hα emission line, our results agree with a strongly increasing EW(Hα) up to $z \sim 2.5$, proportional to $(1+z)^{1.8}$ (see also Fumagalli et al. 2012; Sobral et al. 2014).

This changes at higher redshifts, where we find that the EW(Hα) is evolving less steeply than expected from the extrapolation from lower redshifts. This result is in good agreement with the recent study at $z \sim 4.5$ (Marmol-Queralto et al. 2015; Smit et al. 2015b), based on smaller samples but similar galaxy properties in terms of stellar masses and ages. The results of other studies (Shim et al. 2011; Schenker et al. 2013; Stark et al. 2013; Rasappu et al. 2015)[18] show larger EW(Hα) on average, which we think is due to sample selection. On the one hand, these galaxies are found in the faint tail of the luminosity distribution, and stellar masses quoted for these galaxies are 0.5 dex or more lower than in our sample. On the other hand, in order to be spectroscopically confirmed, these continuum-faint galaxies have to be (strongly) Lyα-emitting and therefore young with high star formation because it is expected that EW(Hα) is positively correlated with age and SFR (e.g., Leitherer et al. 1999; Cowie et al. 2011). We fit the EW(Hα)(z) evolution at $z > 2.5$ (thereby providing the continuity at $z = 2.5$) where no spectroscopic data are available based on our minimally biased COSMOS sample (see Section 5) and find that the evolution of the Hα EW is best described by EW(Hα) $\propto (1+z)^{1.3}$ at these redshifts.

4.2. The sSFR at z > 4

The Hα is a tracer for star formation, and the stellar continuum redward of 4000 Å is a good tracer for stellar mass. Therefore, the Hα EW is directly proportional to the sSFR of a galaxy with the normalization factor depending solely on its internal properties such as metallicity, age of stellar populations, and SFH (e.g., Leitherer et al. 1999; Cowie et al. 2011).

[18] These studies do include [S II] and/or [N II] in their measurements of Hα. We correct, if necessary, the contribution from [S II] and [N II] by assuming a constant factor of 15%, if both, and 5%, if [N II] only.

Table 1
Summary of Observational Data and Best-fit Models

Data and Observations (Spectroscopic)				Model Fit[a]					Input Properties		
				Emission Lines			Dust[c]				
Redshift	Color	$\#<2''$	$\#<3''$	EW(Hα)$_0$[b]	α	ξ	$E(B-V)_0$	$z_{d,0}$	Z ($Z_\odot$)	Age (yr)	SFH
$1.0<z<2.9$	$[H]-[K]$	3571	1671	13.4	2.01	1.1	0.45	0.9	0.020	$T(z)-T(11)$	constant
				5.5	2.96	0.9	0.90	0.85	0.004	$T(z)-T(11)$	constant
				78.1	0.32	1.4	0.45	2.10	0.020	$T(z)-T(11)$	exp. inc.
				57.2	0.72	1.0	0.85	1.40	0.04	$T(z)-T(11)$	exp. inc.
$1.0<z<4.0$	$[K]-[3.6\,\mu m]$	3863	1811	15.8	1.92	0.8	0.70	1.10	0.020	$T(z)-T(11)$	constant
				32.8	1.35	0.6	0.80	1.50	0.004	$T(z)-T(11)$	constant
				10.0	2.34	1.1	0.70	1.60	0.020	$T(z)-T(11)$	exp. inc.
				21.0	1.71	0.7	0.90	1.80	0.004	$T(z)-T(11)$	exp. inc.
$3.0<z<6.0$	$[3.6\,\mu m]-[4.5\,\mu m]$	530	257	9.9	2.01	0.8[d]	0.90	1.25	0.020	$T(z)-T(11)$	constant
				13.6	1.83	0.8[d]	1.10	1.70	0.004	$T(z)-T(11)$	constant
				10.6	1.98	0.9[d]	0.80	1.60	0.020	$T(z)-T(11)$	exp. inc.
				8.5	2.10	0.8[d]	1.20	1.80	0.004	$T(z)-T(11)$	exp. inc.

Notes.
[a] The errors in the resulting EW(Hα) are estimated by a Monte Carlo simulation to be ~30%. The errors in $\xi = ([\mathrm{O\,III}]/\mathrm{H}\alpha)^{-1}$ are similarly estimated to be of the order of 70%.
[b] In angstroms and rest-frame.
[c] Strictly speaking, these parameters include not only dust but also changes in the intrinsic SED that are not included elsewhere in our model.
[d] These are best-fit values, but are more uncertain than at $1.0<z<2.9$ because only part of the wavelength range including [O III] and Hα emission lines is covered by our data. The actual scatter in these measurements will be discussed in more detail in Section 4.3.

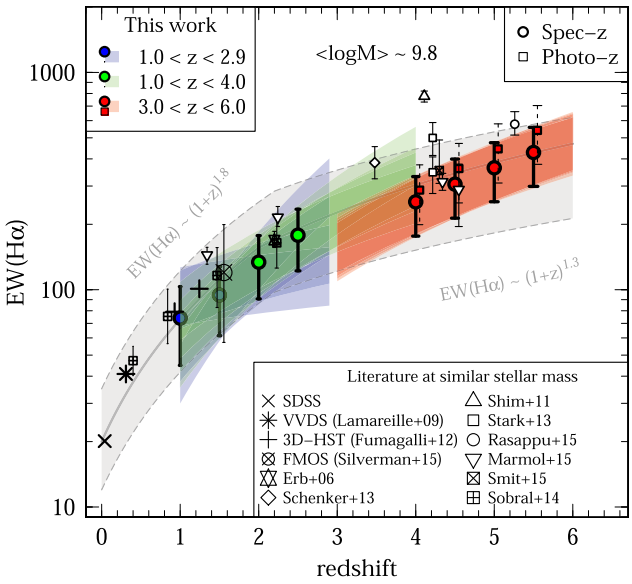

Figure 5. Mean rest-frame EW(Hα) as a function of redshift. Our results in the three different redshift windows are shown in blue ($1.0<z<2.9$), green ($1.0<z<4.0$), and red ($3.0<z<6.0$). The different bands show the four combinations of metallicity and SFHs for each window (see text). The colored points show the redshifts where the Hα line is directly accessible. The red squares show the same for a sample based on photometric redshifts at $z>3$. The symbols (see legend) show different studies measuring EW(Hα) directly from spectra or narrow bands (Erb et al. 2006; Lamareille et al. 2009; Fumagalli et al. 2012; Sobral et al. 2014; Silverman et al. 2015b) or from observed color or SED fitting (Shim et al. 2011; Schenker et al. 2013; Stark et al. 2013; Marmol-Queralto et al. 2015; Rasappu et al. 2015; Smit et al. 2015b). To homogenize the results, we apply a constant factor of 15% (5%) to the literature measurements to correct for the [N II] and [S II] ([N II] only) emission lines where necessary.

The ensemble approach also allows a clear determination of the average and range of these properties and allows their propagation (forward-modeling) to the final results. This is one big advantage over a model based on "galaxy-by-galaxy" fitting. Furthermore, remember that our results are mostly insensitive to SFH, age, and metallicities at redshifts $z>4$ where the age of the universe is less than 1 Gyr (see Figure 3).

In order to convert the EW(Hα) to sSFR, we use the composite stellar population models of Bruzual & Charlot (2003) bracketing different SFHs (exponentially increasing with $\tau = 5\times10^8$ yr and constant). These models are normalized by stellar mass and we can therefore directly convert EW(Hα) into a *specific* Hα luminosity without any additional measurement of stellar mass. We then use the relation of Kennicutt & Evans (2012) (assuming a Chabrier IMF) to convert the specific Hα luminosity into a specific SFR. Figure 6 shows the resulting sSFR(z) derived from our EW(Hα) evolution with redshift along with various measurements from the literature. The orange shaded band (and solid orange line) shows the sSFR derived based on the exponentially increasing SFH, while the hatched band shows the case of a constant SFH. For both we assume an age evolution corresponding to the cosmic time elapsed since $z=11$. The case for a constant age of 500 Myr (and exponentially increasing SFH) is shown as a dashed orange line.

Since it is directly calculated from the EW(Hα), the sSFR evolution with redshift is different at low and high redshifts. While we find a strong increase of sSFR proportional to $(1+z)^{2.4}$ at $z\lesssim2.2$, this flattens out to a redshift dependence of $(1+z)^{1.5}$ at $z\gtrsim2.2$.

For comparison, the symbols show various measurements from the literature, which are summarized in Table 2 (low

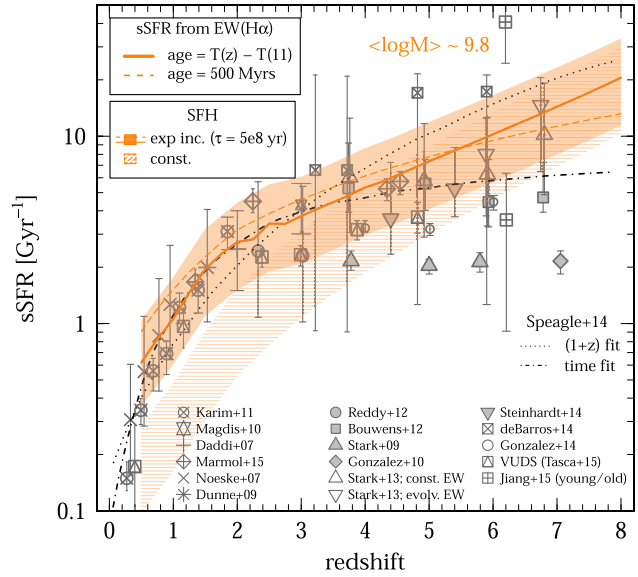

Figure 6. Evolution of sSFR as a function of redshift computed from EW(Hα)(z) in the range $0.5 < z < 8.0$ (orange, extrapolated below $z = 0.5$ and above $z = 6$). The orange band assumes an exponentially increasing SFH ($\tau = 5 \times 10^8$ yr) and evolving age (Hubble time since $z = 11$). The width of the band includes a range in metallicity (0.2–1.0 $Z_\odot$) and the range in EW(Hα). The orange dashed line shows the case for a fixed age of 500 Myr. The hatched band shows the same for a constant SFH. Along with this, we show observations at low z (Daddi et al. 2007; Noeske et al. 2007; Dunne et al. 2009; Magdis et al. 2010; Karim et al. 2011; Reddy et al. 2012) and high z without emission line correction (Stark et al. 2009; González et al. 2010; Bouwens et al. 2012a) and with emission line correction (Stark et al. 2013; de Barros et al. 2014; González et al. 2014; Steinhardt et al. 2014; Jiang et al. 2016; Marmol-Queralto et al. 2015; Tasca et al. 2015). The dotted (dotted–dashed) line shows the fit from Speagle et al. (2014) parameterized in redshift (time) space. We find the sSFR to be proportional to $(1 + z)^{2.4}$ at $z < 2.2$ and proportional to $(1 + z)^{1.5}$ at higher redshifts, indicative of a flattening.

redshift) and Table 3 (high redshift). These measurements can be broadly split into three groups: (i) measurements at $z \lesssim 3$, which are based on reliable SFR indicators in the far-IR or submillimeter and without the problem of emission line contamination (Daddi et al. 2007; Noeske et al. 2007; Dunne et al. 2009; Magdis et al. 2010; Karim et al. 2011; Reddy et al. 2012), (ii) measurements at $z > 3$ that are based on SFR from UV and SED fitting as well as stellar mass estimates *not* corrected for emission lines (Stark et al. 2009; González et al. 2010; Bouwens et al. 2012a), and (iii) measurements at $z > 3$ that are based on SFR from UV and SED fitting as well as stellar mass estimates corrected for emission lines (Stark et al. 2013; de Barros et al. 2014; González et al. 2014; Steinhardt et al. 2014; Jiang et al. 2016; Marmol-Queralto et al. 2015; Salmon et al. 2015; Tasca et al. 2015). We note that the SFRs at $z > 3$ are predominantly determined from the rest-UV, which is affected by dust. Assuming that the stellar masses (determined from the rest-frame near- and mid-IR) are little affected by dust, the derived sSFR depends on the assumed attenuation curve, which is in most cases that of Calzetti et al. (2000). For $E(B - V) = 0.2$ (upper limit at $z > 3$), we expect the SFR (and therefore sSFR) determined from the rest-UV to be ~30% larger if a dust attenuation curve similar to that of the Small Magellanic Cloud (SMC) is used.

4.3. The [O III]/Hα Ratio at z ~ 6

The ratio between Hα and Hβ depends solely on the dust attenuation. Since we do fit Hα and dust attenuation, we can directly compute Hβ and thus separate it from the [O III] line. This allows us to directly measure the ratio of [O III] to Hα in three discrete redshift ranges centered on $z \sim 2.2$, $z \sim 3.3$, and $z \sim 5.5$ (see Figure 2).

We are able to fit the [O III]/Hα ratio reliably at $z \sim 2.2$ and $z \sim 3.3$, since the redshift range at which the broad-band filters include Hα and [O III] is fully covered by our data (see Figures 2 and 4). The right panel of Figure 7 shows our [O III]λ5007/Hα ratio[19] at $z \sim 2.2$ and $z \sim 3.3$ in blue and green, respectively, along with spectroscopically determined ratios (Steidel et al. 2014; Sanders et al. 2016), which we find to be in excellent agreement with our measurements at $z \sim 2.2$. The different bands for each color again show the four combinations of intrinsic properties in our model.

At $z \sim 5.5$ our data include only galaxies up to $z \sim 5.8$ and therefore do not cover the full redshift range (i.e., entry and exit of [O III] in the 3.6 μm band) that is needed to reliably constrain the [O III]/Hα ratio. Furthermore, the sparse sampling of data at these redshifts contributes to the uncertainty. Also the addition of galaxies with photometric redshifts does not increase the sample size by much at $z > 5.8$, as shown in Appendix A. We therefore discuss this case in more detail in the following. The left panel in Figure 7 shows the redshift range from which we determine the [O III]/Hα ratio at $z \sim 5.5$. As before, the points show the data and the blue band shows their scatter. The model without emission lines (but including dust) is shown as a red dashed line. Note that at these redshifts, where the stellar ages are <1 Gyr, the model is very insensitive to SFH, age, and metallicity and depends primarily on the [O III]/Hα ratio in this case. We show the best-fit [O III]/Hα ratio ($\log([\mathrm{O\,III}]/\mathrm{H}\alpha) \sim 0.0$) along with five different models with increasing ratios in red. This large variation over a range of 1.0 dex in [O III]/Hα indicates the existence of galaxies with very strong [O III] emission at these redshifts, in agreement with the recent findings at $z \sim 6.7$ using a similar technique (e.g., Roberts-Borsani et al. 2015). The galaxies clustering around $z \sim 5.65$ are selected by Lyα narrow band and thus preferentially young and highly star-forming. This could be the reason for their high [O III]/Hα ratios. The range of [O III]/Hα ratios at $z \sim 5.5$ is shown in red on the right panel of Figure 7. Since [O III] and Hβ are not resolved by our method, the [O III]/Hα ratio depends on the uncertainty in dust and the assumed dust attenuation law. We estimate that an uncertainty in dust of $\Delta E(B - V) = 0.1$ together with either a Calzetti or SMC dust attenuation law leads to not more than 20% (or 0.08 dex) variation in the [O III]/Hα ratio.

We find a progressively increasing [O III]λ5007/Hα ratio with redshift at $z > 2$, once the large upward scatter at $z \sim 6$ is taken into account. On the other hand, there is not much evolution between $z \sim 1$ and $z \sim 2$ (literature at $z \sim 1$ and $z \sim 1.5$, Colbert et al. 2013; Mehta et al. 2015; Silverman et al. 2015b). The average line ratio of local ($z \lesssim 0.3$) SDSS galaxies is ~0.2 dex lower than at $z = 2$ and ~0.2–0.8 dex lower than at $z \sim 6$. However, the distribution of [O III]λ5007/Hα ratios in local galaxies (shown by the dashed density histogram) is broad and subsamples of these galaxies show

[19] We split the [O III] doublet (4960 and 5007 Å) by assuming [O III] λ5007 = 1/3 × [O III]λ4960.

Table 2
Literature on sSFR Measurements at Low Redshift

Sample		Measurements			
z	# Galaxies	SFR ($M_\odot$ yr^{-1})	M ($M_\odot$)	Emission Lines	Reference
$1.4 < z < 2.5$	1300[a,b]	different estimators (UV, far-IR, 1.4 GHz)	SED fitting	none	Daddi et al. (2007)
$0.2 < z < 1.1$	~2900[a]	optical emission lines and 24 μm	SED fitting	none	Noeske et al. (2007)
$0.2 < z < 3$	~23.000[b]	stacked 1.4 GHz	SED fitting	none	Dunne et al. (2009)
$z \sim 3$	248[a]	UV	SED fitting	none	Magdis et al. (2010)
$0.2 < z < 3$	$>10^5$[b]	stacked 1.4 GHz	SED fitting including 24 μm	none	Karim et al. (2011)
$1.4 < z < 3.7$	~300[a]	SED, UV, and 24 μm	SED fitting	none	Reddy et al. (2012)

Notes.
[a] Spectroscopic sample.
[b] Photometric sample.

similar line ratios to high-z galaxies. The potential of such "local high-z analogs" is further discussed in Section 5.4.

5. DISCUSSION

We use a sample of >500 spectroscopically confirmed galaxies to derive the Hα EW, the sSFR(z), and the [O III] λ5007/Hα ratio at $3 < z < 6$. The main idea of our analysis is to base these measurements on primary observables (the observed color versus redshift evolution) and to minimize the model uncertainties. The forward-modeling approach based on the ensemble instead of single galaxies allows us to marginalize over a range of SFH, metallicities, and ages and to propagate the uncertainties in these quantities to the final result. Due to the young age of the universe of less than 1 Gyr at $z > 4$, the differences between different assumptions that go into the modeling of the galaxy population are less significant, leading to robust results at these high redshifts (see also Figure 3).

In the previous section, we have established the following results.

1. The EW(Hα) increases continuously as $(1+z)^{1.8}$ up to $z \sim 2.5$ and flattens off at higher redshifts with a redshift proportionality of $(1+z)^{1.3}$.
2. The sSFR increases proportionally to $(1+z)^{2.4}$ at $z \lesssim 2.2$ but shows a less strong evolution at higher redshifts proportional to $(1+z)^{1.5}$.
3. We find a best-fit [O III]/Hα ratio of $z \sim 6$ star-forming galaxies of the order of unity (similar to $z = 2$ and $z = 3$ galaxies), but with a scatter up to a ratio of five. This suggests the progressively increasing [O III]/Hα ratios at $z > 3$.

Before proceeding to the discussion of these results, we have to make sure that our sample is only minimally biased.

5.1. How Strong are the Biases in Our Sample?

The emission line properties of galaxies vary substantially between different samples. This has a direct implication for the sSFR, since galaxies with strong emission lines tend to be young and strongly star-forming. In particular, spectroscopic high-z samples are often selected by emission line and color and are therefore biased toward young, star-forming galaxies.

The position of individual galaxies in our sample at $z > 3$ on the plane of stellar mass versus SFR is in good agreement with the expected average star-forming main sequence extrapolated from measurements at lower redshifts that are based on reliable IR SFR indicators (e.g., Lee et al. 2015; Schreiber et al. 2015). This is also verified by direct determination of the main sequence at higher redshifts (Steinhardt et al. 2014). However, this comparison has to be taken with a grain of salt as there are large uncertainties in the measurement of stellar masses and SFR from SED fitting for individual galaxies at high redshifts. We therefore proceed with two additional tests to quantify possible biases in our sample.

The VUDS sample is selected purely by photometric redshifts and is therefore less affected by the "spectroscopic bias" than the COSMOS sample, which is partially selected by color. If the latter is severely biased, we would expect a non-negligible change in our results when removing the VUDS galaxies. However, this is not confirmed, which indicates that the biases are minimal. We can even go one step further and select galaxies purely on their photometric redshift from the *COSMOS2015* catalog. In this case, we do not expect any spectroscopic bias; on the other hand, these galaxies are obviously not spectroscopically confirmed and the photometric uncertainties tend to wash out the wiggles in the color versus redshift relation. We therefore apply a strict selection on the photometric redshift errors as detailed in Appendix A. We perform the same analysis as for the spectroscopic sample and do not see significant differences in the results. As shown in Figure 5 for $z > 3$, the Hα EWs of the photometric sample are in good agreement with the determination from the spectroscopically selected samples. The slightly higher EW(Hα) of the photometric sample could be explained by increased photometric redshift uncertainties of galaxies with weak emission lines. Such galaxies are less likely to pass our selection criteria as discussed above.

From these various tests, we conclude that our total sample is minimally biased and represents well the average galaxy population at these redshifts and stellar masses. With this in hand, we continue to discuss the results obtained in the previous section.

5.2. Broken sSFR Evolution and the Importance of Major Mergers

The sSFR of the average star-forming galaxy population is critical to understand galaxy formation in the high-redshift universe. Different views of the evolution of sSFR at high redshifts exist not only between theoretical predictions and observations, but also among observations themselves. In particular, cosmological, hydrodynamical simulations predict a steep, continuous increase of sSFR over the whole redshift range up to very high redshifts. For example, an increase

Table 3
Literature on sSFR Measurements at High Redshift

Sample		Measurements				
z	# Galaxies	SFR ($M_\odot$ yr^{-1})	M ($M_\odot$)	Emission Lines	Comments	Reference
			This Work			
$1 < z < 6$	~3600[a]	(specific) Hα luminosity	…	corrected, direct measurement from observed color	Not involving fitting of stellar mass or SFR from UV. Strongly increasing sSFR at $z < 2.5$ and flattening off at higher redshifts	This work
			Studies *not* including emission lines			
$4 < z < 6$	~800[b]	UV (not corrected for dust)	SED fitting	none	flat sSFR (z) relation, not considering emission lines	Stark et al. (2009)
$z \sim 7$	11[b]	UV	SED fitting	none	flat sSFR (z) relation, not considering emission lines	González et al. (2010)
$4 < z < 7$	~2400[b]	UV	UV mass to light ratios	none	flat sSFR (z) relation, not considering emission lines	Bouwens et al. (2012a)
			Studies including emission lines			
$3.8 < z < 5$	92[a]	UV (corrected for dust and emission lines)	SED fitting	included, obtained from observed color	nebular emission added to SED templates from observed EW(Hα) distribution. Extrapolated to $z \sim 7$ by assuming constant EW(Hα) as well as EW(Hα) $\propto (1+z)^{1.8}$. Find strongly increasing sSFR at $z > 4$	Stark et al. (2013)
$4 < z < 6$	~750[b]	from SFH derived by SED fitting	SED fitting	included, assuming constant EW(Hα) and $\propto(1+z)^{1.52}$ from $z \sim 2$. Emission line contribution subtracted from photometry before fitting.	increasing sSFR (z) for increasing EW(Hα) model	González et al. (2014)
$3 < z < 6$	~1700[b]	from SFH derived by SED fitting	SED fitting	included, proportional to Lyman continuum photon production	strongly increasing sSFR at $z > 4$	de Barros et al. (2014)
$0.1 < z < 5$	~4500[a]	SED fitting	SED fitting	included, proportional to UV photons	shallow evolution of sSFR (z) at $z > 3$	Tasca et al. (2015)
$z \sim 6$	27[a]	UV and Lyα	SED fitting	included, from Lyα	based on bright LBGs and LAEs. Find two populations (split at ages of 30 Myr) with vastly different sSFR	Jiang et al. (2016)
$1.2 < z < 5$	~400[a,b]	Hα luminosity	SED fitting including emission line templates. Use SED SFR to fix Hα flux and other emission lines related to it.	residual from SED fitting (excluding contaminated filters)	shallow evolution of sSFR at $z > 3$.	Marmol-Queralto et al. (2015)

Notes.
[a] Spectroscopic sample.
[b] Photometric sample.

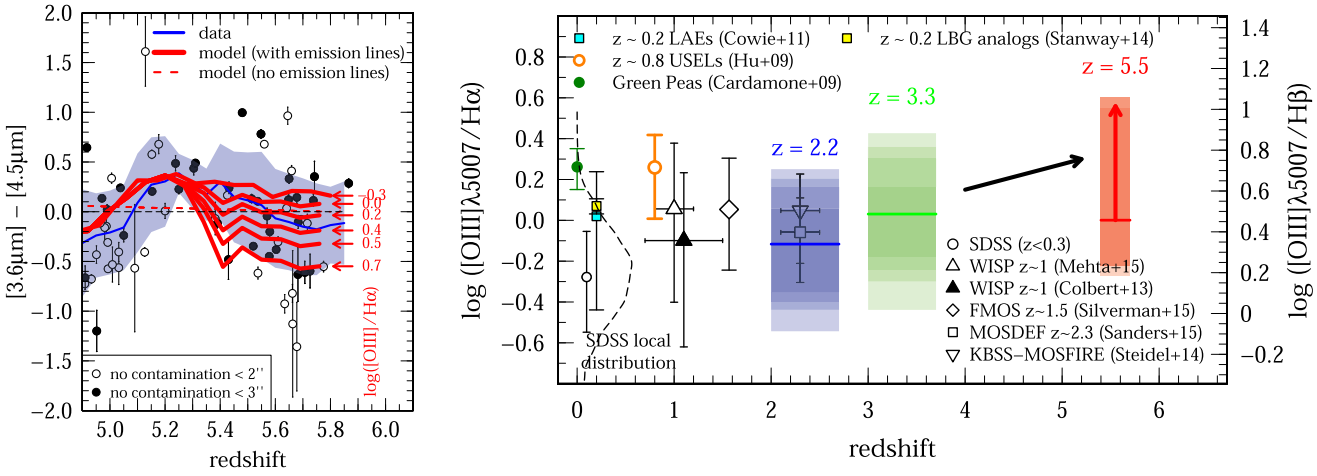

Figure 7. Left: because our data do not have the full redshift range to reliably measure the [O III]/Hα ratio at $z \sim 5.5$, we show here the scatter of this measurement. The top red line with log([O III]/Hα) = 0.0 shows the best-fit model. The other lines show models with increased [O III]/Hα ratios. We find $-0.3 <$ log([O III]/Hα) < 0.7 at $z \sim 5.5$. The data are shown in blue and the model without emission lines is shown as a red dashed line. Right: mean dust-corrected [O III]/Hα ratio as a function of redshift. All the samples are matched in stellar mass and the [O III]/Hβ ratio is computed assuming case (B). Our estimates based on broad-band colors are shown in blue ($z \sim 2.2$), green ($z \sim 3.3$), and red ($z \sim 5.5$) including their uncertainties (from observation and different models). Spectroscopic measurements at lower redshifts are shown with symbols (Cowie et al. 2011; Colbert et al. 2013; Steidel et al. 2014; Mehta et al. 2015; Sanders et al. 2016; Silverman et al. 2015b) and the distribution of SDSS galaxies at $z \sim 0$ is represented by the black dashed line (open circle: median). All in all, we find a progressively increasing [O III]/Hα ratio over the redshift range $z \sim 2$–6. We also show high-z analogs as local "Green Peas" (green filled circle, Cardamone et al. 2009), Lyman break analogs at $z \sim 0.2$ (yellow square, Stanway et al. 2014), and USELs at $z \sim 0.8$ (orange open circle, Hu et al. 2009) for comparison.

proportional to $(1+z)^{2.3}$ is expected in a picture where the galaxy growth is dominated by cold accretion (e.g., Dekel et al. 2009). Other hydrodynamical simulations, although underestimating the sSFR at a given redshift compared to observations, are in favor of a continuously increasing sSFR up to high redshifts with a similarly steep redshift dependence (e.g., Davé et al. 2011; Sparre et al. 2015). Also, a strong redshift dependence with similar exponent is expected if galaxy growth is closely connected to the dark-matter halo assembly (Tacchella et al. 2013). Clearly, the sSFR of the average galaxy population has to increase toward higher redshifts in order to explain the findings of massive ($>10^{11}\,M_\odot$) galaxies found at high redshifts where they only have a couple of hundred million years to grow (e.g., Weinmann et al. 2011; Steinhardt et al. 2014). Due to small sample sizes, biases, and uncertainties in the fitting of stellar masses and SFRs (mostly due to the unknown contribution of emission lines), it is not clear how strong the increase in sSFR actually is at $z > 3$.

Our results clearly show that the redshift evolution of the sSFR is broken. In particular we find a redshift proportionality of $(1+z)^{2.4}$ at $z < 2.2$ and $(1+z)^{1.5}$ at higher redshifts. At low redshifts ($z < 2$), the steep increase in sSFR is in good agreement with the reliable measurements based on the far-IR and submillimeter observations and spectroscopy. At very low redshifts, our model breaks down, resulting in a strong (factor three and more) overestimation of sSFR. This because our method becomes increasingly more dependent on our assumptions on the SFH due to the older ages of the galaxies. This is indicated by the hatched band in Figure 6 showing the case of a constant SFH, which is likely a better representation of the SFH of low-z galaxies than an exponentially increasing SFH. While these two SFHs give similar results at $z > 3$, they diverge substantially toward lower redshifts. Furthermore, with increasing age of the stellar population, the direct proportionality between Hα EW and sSFR is expected to break down.

At $z \sim 2.5$, the sSFR(z) starts to flatten off and decreases the exponent of its redshift dependence from 2.4 to 1.5. However, the flattening is not as strong as suggested by other studies based on SED fitting and taking into account the effect of emission lines, finding a $(1+z)$ exponent close to unity (González et al. 2014; Marmol-Queralto et al. 2015; Tasca et al. 2015). We clearly rule out a flat redshift versus sSFR relation at $z > 3$ as suggested by earlier studies (Stark et al. 2009; González et al. 2010; Bouwens et al. 2012a). These do not take emission lines into account and therefore overestimate the stellar masses by factors of three or more (e.g., Stark et al. 2013), which leads to the same amount of underestimation of their sSFRs. The average sSFR of 8–10 Gyr^{-1} at $z \sim 5$–6 corresponds to an e-folding time for galaxy growth of ~100–200 Myr, which is increased by a factor of two or more at higher redshifts. This is sufficient to explain the observations of galaxies with stellar masses of $\log(M/M_\odot) = 10.5$–11.0 at $z \sim 5$. Even more massive galaxies ($\log(M/M_\odot) > 11.0$) are likely to be formed with the help of major mergers. This is in line with our finding that the redshift evolution of sSFRs at $z > 3$ is less steep than expected from simulation where galaxy growth is dominated by cold gas accretion (e.g., Dekel et al. 2009). We therefore do expect an additional mechanism for their mass growth. Major mergers—important up to high redshifts (e.g., Tasca et al. 2014; Rodriguez-Gomez et al. 2015)—can increase the stellar mass of a galaxy by factors of two per merger without increasing the sSFR over a long timescale.[20]

5.3. BPT diagram at z ~ 6

The strong increase of sSFR shows that star formation at early epochs proceeded at a different pace than in today's galaxies. It is therefore a valid question whether the scaling relations that are used in today's universe still hold for the very first galaxies. In particular, the [N II] abundance, a measure of metallicity, in young high-redshift galaxies is currently

[20] They might increase the sSFR on short timescales by triggering a starburst.

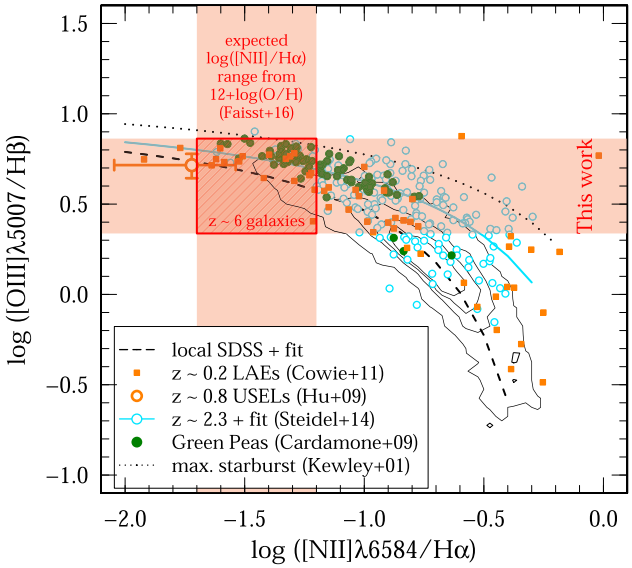

Figure 8. The location of our $z \sim 6$ galaxies (red-hatched square) on the BPT diagram assuming the local [N II]/Hα vs. metallicity relation (Maiolino et al. 2008) and average metallicities of $12 + \log(\mathrm{O/H}) < 8.2$ at $z \sim 6$ (Faisst et al. 2015). Local SDSS galaxies are shown as contours with the best fit (dashed line). We also show LAEs at $z \sim 0.2$ (orange squares, Cowie et al. 2011), USELs at $z \sim 0.8$ (orange point, Hu et al. 2009), $z \sim 2$ galaxies (cyan points and best fit as cyan line, Steidel et al. 2014), and "Green Peas" (green dots, Cardamone et al. 2009). Within our measurement uncertainties, we find the $z \sim 6$ galaxies to lie in the expected region of the BPT diagram; however, our data are not good enough to rule out a [N II] enhancement in high-z galaxies as currently discussed in the literature.

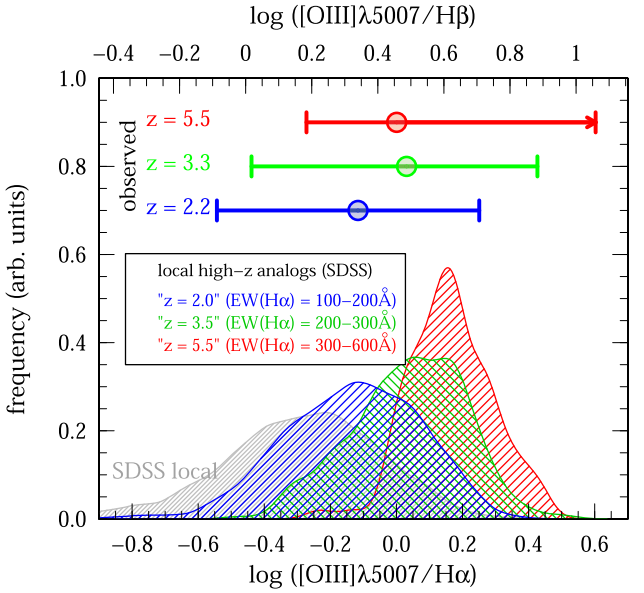

Figure 9. High-z galaxies are "not special." Subsamples of local galaxies in SDSS that match the [O III]λ5007/Hα ratios of high-z galaxies. The local high-z analogs are selected based on EW(Hα), i.e., sSFR, to be similar to galaxies at $z \sim 2$, $z \sim 3.5$, and $z \sim 5.5$. This shows the potential of using local galaxies with high-resolution spectra to investigate the properties of high-z galaxies.

debated. It has been observed that intermediate-redshift galaxies ($z \sim 2$) reside in a different region on the "Baldwin, Phillips & Terlevich" diagram (BPT diagram, Baldwin et al. 1981; Kewley et al. 2013) compared to the majority of local galaxies (see also Figure 8). The BPT diagram connects the [O III]λ5007/Hβ ratio with the [N II]/Hα ratio, the latter being a tracer of the metal content in a galaxy (e.g., Pettini & Pagel 2004; Kewley & Ellison 2008; Maiolino et al. 2008). The offset between high- and low-redshift galaxies is not completely understood yet, and studies argue for a harder stellar ionization field causing an enhanced [O III]λ5007/Hβ ratio or a change in the electron temperature of high-z galaxies (e.g., Steidel et al. 2014). Others are in favor of an enhancement of [N II] abundances in these galaxies with respect to local galaxies (e.g., Masters et al. 2014; Cowie et al. 2016; Shapley et al. 2015). Interestingly, the stars in local globular clusters, which are thought to be formed in the very early universe, also show nitrogen enhancements (e.g., Spite & Spite 1986; Maccarone & Warner 2011). If this is the case, a recalibration of the local relation between [N II]/Hα and metallicity at high redshifts is required.

Although with a large uncertainty, we can test the above directly using our estimates of the [O III]λ5007/Hα ratio at $z \sim 6$. Including the scatter as described in Section 4.3, we find a range $\log([\mathrm{O\,III}]\lambda5007/\mathrm{H}\beta) = 0.35$–$0.85$, which we show on the y-axis of the BPT diagram (Figure 8). In addition, we expect the gas-phase metallicities of our galaxies to be of the order of $12 + \log(\mathrm{O/H}) \sim 8.2 \pm 0.2$ at $\log(M/M_{\odot}) \sim 10.0$ (Faisst et al. 2015). Bluntly assuming that the [N II]/Hα versus metallicity relation holds at these redshifts, we would expect $\log([\mathrm{N\,II}]/\mathrm{H}\alpha)$ between -1.7 and -1.2 (Maiolino et al. 2008), which is shown as a range on the x-axis on the BPT diagram.

As expected from their low metallicities, our $z \sim 6$ galaxies are located (as shown by the red-hatched square) to the left of the locus of average local SDSS galaxies (black contours) as well as the bulk of $z \sim 2$ galaxies (cyan open points, Steidel et al. 2014). On the other hand, they show a good agreement with the "Green Peas" (green dots), which are local galaxies with strong optical emission lines and are often referred to as local high-z analogs (Cardamone et al. 2009). Similarly, they coincide with metal-poor ultrastrong emission line galaxies (USELS) at $z \sim 0.8$ (Kakazu et al. 2007; Hu et al. 2009) and metal-poor strong Lyα emitters (LAEs) at $z \sim 0.2$ (Cowie et al. 2011).

In summary, the $z \sim 6$ galaxies overlap with various high-z analogs at lower redshifts. Assuming similar physics in such galaxies as in high-z galaxies, this indicates that [N II] is a reasonable measure of metallicity at high z. However, there is a lot of room to move and the uncertainties in our measurements are certainly too large to draw final conclusions, and the idea of an enhancement of [N II] in high-z galaxies cannot be rejected.

5.4. Local High-z Analogs

Clearly, as seen in Section 5.3, our efforts to measure the spectral properties of high-z galaxies are limited by the capabilities of the current (near-)IR telescopes. One way to progress is to define samples of local galaxies that resemble high-z galaxies in terms of spectral, photometric, and morphological properties (like "Green Peas" or USELs). These samples, providing high-resolution spectral information, can be used to investigate the emission line properties of high-z galaxies (e.g., on the BPT diagram) and provide useful priors on emission line strengths and ratios to improve the results from SED fitting.

In Figure 9, we show that SDSS galaxies selected by *just* the EW(Hα) (i.e., sSFR), as they are expected at $z \sim 2$, $z \sim 3$, and $z \sim 6$, have similar [O III]λ5007/Hα distributions to high-z

galaxies, i.e., they could serve as high-z analogs. In particular, high-z galaxies are not special in terms of their spectral properties, but they are included in subsamples in the tails of the total distribution of low-z galaxies (shown in gray). This is also in line with local Green Peas (Cardamone et al. 2009), Lyman break analogs at $z < 0.2$ (Stanway et al. 2014), as well as USELS at $z \sim 0.8$ (Cowie et al. 2011), all showing log ([O III]λ5007/Hβ) $\sim$ 0.5–0.7. Finding such local high-z analogs opens doors for investigating the spectral properties and physical relations of high-z galaxies using the high-resolution spectra of galaxies in the local universe, and will be addressed in a future paper.

6. SUMMARY AND CONCLUSIONS

In this paper, we introduce a simple method to measure the spectral properties and sSFRs of the *ensemble* of high-redshift galaxies via *forward-modeling* of their observed color versus redshift evolution. Our method does not require any SED fitting of stellar masses to measure the sSFR. The sSFRs are therefore derived as closely as possible from *primary observations* (the observed color of galaxies). Our ensemble approach allows a consistent modeling of the uncertainties of the various unknown intrinsic galaxy properties (metallicity, age, SFH) and the investigation of their impact on the results. Importantly, it does not depend on the measurement of single galaxies, which is more uncertain. This analysis is made possible only through the very large spectroscopic sample available on COSMOS, since accurate spectroscopic redshifts are necessary to get an accurate color versus redshift relation.

Summarizing, these are our final conclusions.

1. We show that we are able to determine the spectral properties and subsequently the sSFR(z) at $z > 4$ from primary observations with very small uncertainties from modeling. This allows us to put important and reliable constraints on the physics of the first galaxies in the universe.
2. The sSFR increases proportionally to $(1+z)^{2.4}$ at $z < 2.2$ and proportionally to $(1+z)^{1.5}$ at higher redshifts. This indicates a fast build-up of stellar mass in galaxies at $z > 3$ within e-folding times of 100–200 Myr. The redshift evolution at $z > 2.2$ cannot be explained solely by growth driven by cold accretion.
3. We find a tentative increase in the [O III]λ5007/Hβ ratio between $z \sim 2$ and $z \sim 6$, but this has to be confirmed by larger samples at $z > 5$.
4. Taking at face value the [O III]λ5007/Hβ ratio and assuming the [N II]/Hα versus metallicity relation of local galaxies, we find $z \sim 6$ galaxies to reside at a similar location on the BPT diagram as the "Green Peas" as well as metal-poor USELs and LAEs. Our data do not allow us to draw further conclusions on a possible [N II] enhancement in high-z galaxies as is currently being debated.
5. High-z analogs can be selected from the tail distribution of local SDSS galaxies by matching in sSFR. Local galaxies are therefore a powerful tool to investigate the spectral (and physical) properties of high-z galaxies and also provide useful priors on emission line strengths that can be used to improve the SED fitting.

The spectral properties of high-z galaxies will ultimately be tested by the IR capability of the next generation of telescopes, most importantly the *James Webb Space Telescope*, currently scheduled for launch in 2018. Our sample provides a useful test-bed.

We would like to thank Josh Speagle, Micaela Bagley, and Bahram Mobasher for valuable discussions. We also would like to thank the referee for valuable comments that have improved this paper. A.F. acknowledges support from the Swiss National Science Foundation. C.L. is supported by the ILP LABEX (under reference ANR-10-LABX-63 and ANR-11-IDEX-0004-02). J.D.S. is supported by JSPS KAKENHI Grant Number 26400221, the World Premier International Research Center Initiative (WPI), MEXT, Japan and by CREST, JST. Part of this work is based on data obtained with the European Southern Observatory Very Large Telescope, Paranal, Chile, under Large Programs 175.A-0839 and 185.A-0791. This work is supported by funding from the European Research Council Advanced Grant ERC-2010-AdG-268107-EARLY. Based on data products from observations made with ESO Telescopes at the La Silla Paranal Observatory under ESO programme ID 179.A-2005 and on data products produced by TERAPIX and the Cambridge Astronomy Survey Unit on behalf of the UltraVISTA consortium. Also, the authors wish to recognize and acknowledge the very significant cultural role and reverence that the summit of Mauna Kea has always had within the indigenous Hawaiian community. We are most fortunate to have the opportunity to conduct observations from this mountain.

APPENDIX A
COMPARISON TO PHOTO-z SAMPLE OF GALAXIES AT $z > 3$

Spectroscopically selected galaxy samples at high redshift ($z \gtrsim 4$) could be biased toward young, star-forming galaxies with strong Lyα emission that would increase EW(Hα) and sSFR compared to the average population. However, due to the target selection of our spectroscopic samples (especially the VUDS sample, the selection of which is based on photometric redshifts) we do not expect severe biases. We can (at least partly) assess the severity of biases at $3 < z < 6$ by comparing our sample to photometrically selected galaxies.

For the investigation of the observed color versus redshift relation, we need a clean sample of photometrically selected galaxies. The basis of our sample builds on the *COSMOS2015* photometric catalog, containing photometric redshifts that are derived with more than 30 filters including broad, intermediate, and narrow bands. The photometric redshifts are verified with large numbers of spectroscopically confirmed galaxies and show an accuracy of better than ~5% on average (see Laigle et al. 2016). We select a clean sample of galaxies by requiring 68% of the probability distribution function within $3 < z < 6$ and a redshift uncertainty less than 5%. The former rejects galaxies with a considerable second redshift solution at $z < 3$ and the latter results in $\Delta z \leqslant 0.27$ in this redshift range, which is enough to resolve the "wiggles" in the color versus redshift relation caused by emission lines. We reject galaxies that have companions within $2''$ as in the case of the spectroscopic sample. Finally, we adjust the stellar mass range of the photometric sample to be similar to that of the spectroscopic sample at $z > 3$ ($\langle \log(M/M_\odot) \rangle \sim 9.8$).

The top panel in Figure 10 shows the observed color versus redshift evolution for our photometric galaxy sample in the

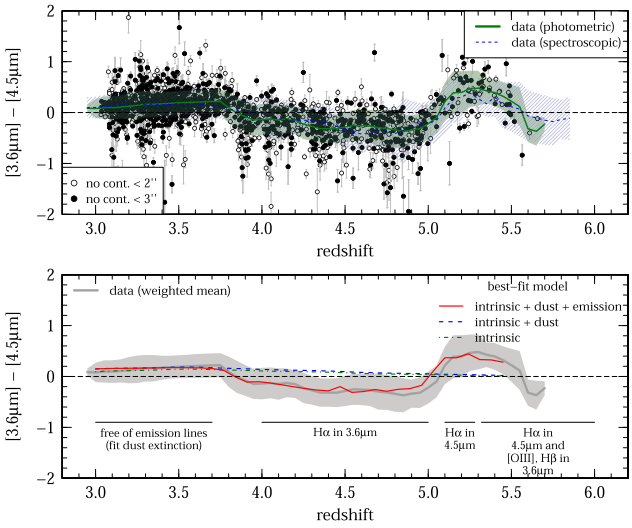

Figure 10. Same as Figure 4 but for galaxies selected by their photometric redshift at $3 < z_{\rm phot} < 6$ (see text). The blue hatched region shows the median color from the spectroscopic sample. The green band shows the median color from the photometric sample, which is in agreement with the spectroscopic one within 1σ. This shows that there are no significant biases in our spectroscopic sample.

range $3 < z_{\rm phot} < 6$ in green. The weighted mean of the spectroscopic sample is shown in blue. We already see that the distributions are very similar. As for the spectroscopic sample, we fit our multi-component model to the observed color. The example of the best-fit model for a constant SFH with solar metallicity is shown in the bottom panel of Figure 10 in red. The resulting EW(Hα)(z) is in good agreement with that obtained from the spectroscopic sample (see Figure 5). All in all, we conclude that our sample is minimally biased and represents well the average population of galaxies at $z > 3$.

APPENDIX B
OBSERVED COLOR VERSUS REDSHIFT EVOLUTION AT $1 < z < 4$

The redshift windows (A) ($1.0 < z < 2.9$) and (B) ($1 < z < 4$) are used to verify our method. The results are compared to EW(Hα) measurements directly based on spectroscopic observations. In Figure 11, we show the same plots as Figure 4 for these redshift windows.

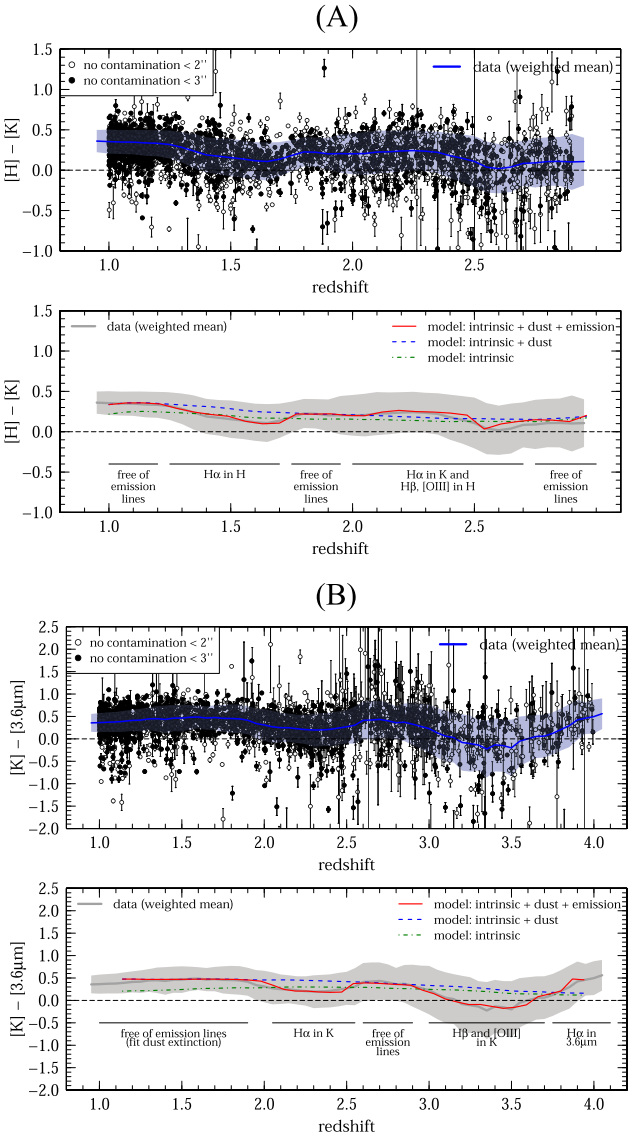

Figure 11. Same as Figure 4 but for redshift windows (A) ($1.0 < z < 2.9$) and (B) ($1 < z < 4$). Top panels: observed color vs. redshift relation. The open (filled) symbols denote galaxies with no contamination from companions within a radius of $2''$ ($3''$) in ACS/F18W and ground-based data. The blue line shows the weighted mean relation with scatter (light blue band) for galaxies with no companion within $2''$. Bottom panels: the best-fit intrinsic (green, dotted–dashed), intrinsic + dust (blue, dashed), and best-fit (red, solid) model.

REFERENCES

Anders, P., Fritze, V., & Alvensleben, U. 2003, A&A, 401, 1063
Baldwin, J. A., Phillips, M. M., & Terlevich, R. 1981, PASP, 93, 5
Bouwens, R. J., Illingworth, G. D., Oesch, P. A., et al. 2012a, ApJL, 752, L5
Bouwens, R. J., Illingworth, G. D., Oesch, P. A., et al. 2012b, ApJ, 754, 83
Bouwens, R. J., Illingworth, G. D., Oesch, P. A., et al. 2014, ApJ, 793, 115
Brammer, G. B., van Dokkum, P. G., Franx, M., et al. 2012, ApJS, 200, 13
Bruzual, G., & Charlot, S. 2003, MNRAS, 344, 1000
Calzetti, D., Armus, L., Bohlin, R. C., et al. 2000, ApJ, 533, 682
Capak, P., Aussel, H., Ajiki, M., et al. 2007, ApJS, 172, 99
Capak, P. L., Carilli, C., Jones, G., et al. 2015, Natur, 522, 455
Cardamone, C., Schawinski, K., Sarzi, M., et al. 2009, MNRAS, 399, 1191
Chabrier, G. 2003, PASP, 115, 763
Colbert, J. W., Teplitz, H., Atek, H., et al. 2013, ApJ, 779, 34
Cowie, L. L., Barger, A. J., & Hu, E. M. 2011, ApJ, 738, 136
Cowie, L. L., Barger, A. J., & Songaila, A. 2016, ApJ, 817, 57
Cullen, F., Cirasuolo, M., McLure, R. J., Dunlop, J. S., & Bowler, R. A. A. 2014, MNRAS, 440, 2300
Daddi, E., Dickinson, M., Morrison, G., et al. 2007, ApJ, 670, 156
Davé, R., Oppenheimer, B. D., & Finlator, K. 2011, MNRAS, 415, 11
de Barros, S., Reddy, N., & Shivaei, I. 2015, ApJ, in press (arXiv:1509.05055)
de Barros, S., Schaerer, D., & Stark, D. P. 2014, A&A, 563, A81
Dekel, A., Birnboim, Y., Engel, G., et al. 2009, Natur, 457, 451
Dunlop, J. S., Rogers, A. B., McLure, R. J., et al. 2013, MNRAS, 432, 3520
Dunne, L., Ivison, R. J., Maddox, S., et al. 2009, MNRAS, 394, 3
Erb, D. K., Steidel, C. C., Shapley, A. E., et al. 2006, ApJ, 647, 128
Faisst, A. L., Capak, P. L., Davidzon, I., et al. 2015, ApJ, submitted (arXiv:1512.00018)
Fumagalli, M., Patel, S. G., Franx, M., et al. 2012, ApJL, 757, L22
González, V., Bouwens, R., Illingworth, G., et al. 2014, ApJ, 781, 34
González, V., Labbé, I., Bouwens, R. J., et al. 2010, ApJ, 713, 115
Hayes, M., Schaerer, D., Östlin, G., et al. 2011, ApJ, 730, 8
Hsieh, B.-C., Wang, W.-H., Yan, H., et al. 2012, ApJ, 749, 88
Hu, E. M., Cowie, L. L., Kakazu, Y., & Barger, A. J. 2009, ApJ, 698, 2014
Ilbert, O., Arnouts, S., McCracken, H. J., et al. 2006, A&A, 457, 841
Ilbert, O., McCracken, H. J., Le Fèvre, O., et al. 2013, A&A, 556, A55
Jiang, L., Finlator, K., Cohen, S. H., et al. 2016, ApJ, 816, 16

Kakazu, Y., Cowie, L. L., & Hu, E. M. 2007, ApJ, 668, 853
Karim, A., Schinnerer, E., Martínez-Sansigre, A., et al. 2011, ApJ, 730, 61
Kashino, D., Silverman, J. D., Rodighiero, G., et al. 2013, ApJL, 777, L8
Kennicutt, R. C., & Evans, N. J. 2012, ARA&A, 50, 531
Kewley, L. J., Dopita, M. A., Leitherer, C., et al. 2013, ApJ, 774, 100
Kewley, L. J., & Ellison, S. L. 2008, ApJ, 681, 1183
Khostovan, A. A., Sobral, D., Mobasher, B., et al. 2015, MNRAS, 452, 3948
Laigle, C., McCracken, H. J., Ilbert, O., Hsieh, P., & Capak, P. 2016, ApJ, submitted
Lamareille, F., Brinchmann, J., Contini, T., et al. 2009, A&A, 495, 53
Le Fèvre, O., Amorin, R., Bardelli, S., et al. 2014, Msngr, 155, 37
Le Fèvre, O., Saisse, M., Mancini, D., et al. 2003, Proc. SPIE, 4841, 1670
Le Fèvre, O., Tasca, L. A. M., Cassata, P., et al. 2015, A&A, 576, A79
Le Fèvre, O., Vettolani, G., Garilli, B., et al. 2005, A&A, 439, 845
Lee, N., Sanders, D. B., Casey, C. M., et al. 2015, ApJ, 801, 80
Leitherer, C., Schaerer, D., Goldader, J. D., et al. 1999, ApJS, 123, 3
Maccarone, T. J., & Warner, B. 2011, MNRAS, 410, L32
Magdis, G. E., Elbaz, D., Daddi, E., et al. 2010, ApJ, 714, 1740
Maiolino, R., Nagao, T., Grazian, A., et al. 2008, A&A, 488, 463
Mannucci, F., Cresci, G., Maiolino, R., et al. 2009, MNRAS, 398, 1915
Marmol-Queralto, E., McLure, R. J., Cullen, F., et al. 2015, MNRAS, submitted (arXiv:1511.01911)
Masters, D., McCarthy, P., Siana, B., et al. 2014, ApJ, 785, 153
McCracken, H. J., Milvang-Jensen, B., Dunlop, J., et al. 2012, A&A, 544, A156
Mehta, V., Scarlata, C., Colbert, J. W., et al. 2015, ApJ, 811, 141
Noeske, K. G., Weiner, B. J., Faber, S. M., et al. 2007, ApJL, 660, L43
Oke, J. B., & Gunn, J. E. 1983, ApJ, 266, 713
Pettini, M., & Pagel, B. E. J. 2004, MNRAS, 348, L59
Planck Collaboration, Ade, P. A. R., Aghanim, N., et al. 2015, arXiv:1502.01589
Rasappu, N., Smit, R., Labbe, I., et al. 2015, MNRAS, submitted (arXiv:1509.02167)
Reddy, N., Dickinson, M., Elbaz, D., et al. 2012, ApJ, 744, 154
Roberts-Borsani, G. W., Bouwens, R. J., Oesch, P. A., et al. 2015, ApJ, in press (arXiv:1506.00854)
Rodriguez-Gomez, V., Genel, S., Vogelsberger, M., et al. 2015, MNRAS, 449, 49
Salmon, B., Papovich, C., Finkelstein, S. L., et al. 2015, ApJ, 799, 183
Sanders, R. L., Shapley, A. E., Kriek, M., et al. 2016, ApJ, 816, 23
Schaerer, D., & de Barros, S. 2009, A&A, 502, 423
Schenker, M. A., Ellis, R. S., Konidaris, N. P., & Stark, D. P. 2013, ApJ, 777, 67
Schreiber, C., Pannella, M., Elbaz, D., et al. 2015, A&A, 575, A74
Scoville, N., Aussel, H., Brusa, M., et al. 2007, ApJS, 172, 1
Scoville, N., Sheth, K., Aussel, H., et al. 2016, ApJ, 820, 83
Shapley, A. E., Reddy, N. A., Kriek, M., et al. 2015, ApJ, 801, 88
Shim, H., Chary, R.-R., Dickinson, M., et al. 2011, ApJ, 738, 69
Shivaei, I., Reddy, N. A., Steidel, C. C., & Shapley, A. E. 2015, ApJ, 804, 149
Silverman, J. D., Daddi, E., Rodighiero, G., et al. 2015a, ApJL, 812, L23
Silverman, J. D., Kashino, D., Sanders, D., et al. 2015b, ApJS, 220, 12
Skelton, R. E., Whitaker, K. E., Momcheva, I. G., et al. 2014, ApJS, 214, 24
Smit, R., Bouwens, R. J., Franx, M., et al. 2015a, ApJ, 801, 122
Smit, R., Bouwens, R. J., Labbé, I., et al. 2015b, ApJ, submitted (arXiv:1511.08808)
Sobral, D., Best, P. N., Smail, I., et al. 2014, MNRAS, 437, 3516
Sparre, M., Hayward, C. C., Springel, V., et al. 2015, MNRAS, 447, 3548
Speagle, J. S., Steinhardt, C. L., Capak, P. L., & Silverman, J. D. 2014, ApJS, 214, 15
Spite, F., & Spite, M. 1986, A&A, 163, 140
Stanway, E. R., Eldridge, J. J., Greis, S. M. L., et al. 2014, MNRAS, 444, 3466
Stark, D. P., Ellis, R. S., Bunker, A., et al. 2009, ApJ, 697, 1493
Stark, D. P., Schenker, M. A., Ellis, R., et al. 2013, ApJ, 763, 129
Steidel, C. C., Rudie, G. C., Strom, A. L., et al. 2014, ApJ, 795, 165
Steinhardt, C. L., Capak, P., Masters, D., & Speagle, J. S. 2015, ApJ, in press (arXiv:1506.01377)
Steinhardt, C. L., & Speagle, J. S. 2014, ApJ, 796, 25
Steinhardt, C. L., Speagle, J. S., Capak, P., et al. 2014, ApJL, 791, L25
Tacchella, S., Trenti, M., & Carollo, C. M. 2013, ApJL, 768, L37
Tasca, L. A. M., Le Fèvre, O., Hathi, N. P., et al. 2015, A&A, 581, A54
Tasca, L. A. M., Le Fèvre, O., López-Sanjuan, C., et al. 2014, A&A, 565, A10
van Dokkum, P., Brammer, G., Nelson, E., et al. 2011, ApJ, 743, 15
Weinmann, S. M., Neistein, E., & Dekel, A. 2011, MNRAS, 417, 2737